

COVER PAGE

Document downloaded by @DAEL

Sat Nov 28 19:39:42 2026
For personal use

When automatic English translation is provided, only the original document is authentic.
The EAA cannot be held responsible of any translation error

Bibliographical reference

SH-wave scattering in the orthotropic half-plane weakened by cavities using BIEM, Petia Dineva, George Manolis, Tsviatko Rangelov and Frank Wuttke, Acta Acustica **vol. 100** (Number 2), 2014, pp. 266-276

DOI
https://doi.org/10.3813/AAA.918706

Acta Acustica united with Acustica
Vol. 100 (2014) 266 – 276

DOI 10.3813/AAA.918706

SH-wave scattering in the orthotropic half-plane weakened by cavities using BIEM

Petia Dineva[1], George Manolis[2], Tsviatko Rangelov[3], Frank Wuttke[4]

[1] Institute of Mechanics, Bulgarian Academy of Sciences, Sofia 1113, Bulgaria

[2] Department of Civil Engineering, Aristotle University, Thessaloniki, GR 54124, Greece

[3] Institute of Mathematics and Informatics, Bulgarian Academy of Sciences, Sofia 1113, Bulgaria

[4] Chair of Marine and Land Geomechanics, Christian-Albrechts-University Kiel, 24118 Kiel, Germany.
fw@gpi.uni-kiel.de

Summary

A basic problem of elastodynamics, namely the anisotropic half-plane weakened by cavities of arbitrary shape and swept by upward moving, time harmonic SH-waves is considered here. The method of analysis used is the boundary integral equation method, in both displacement and non- hypersingular traction forms, which is based on Green's function for a point harmonic load in the elastic, homogeneous and anisotropic (orthotropic) half-plane. This type of function is derived in closed form using the Radon transformation and does not require modeling the traction-free horizontal surface. Instead, only the buried cavity surfaces are discretized using a parabolic approximation of the field variables over a given boundary element. Numerical solution is then realized through standard nodal collocation. Following an extensive validation study for the proposed numerical methodology against existing analytical or semi-analytical solutions, a comprehensive number of simulations are conducted to investigate the dependence of the scattered wave field on key problem parameters.

PACS no. 43.40.-r

1. Introduction

This work presents a non-conventional boundary integral equation method (BIEM) solution of time harmonic problems in elastodynamics, where the anisotropic elastic half-plane containing cavities is subjected to incident SH-waves. This problem is of interest in the seismic response of complex geological regions with large underground structures such as reservoirs and tunnels, because information on their dynamic behavior and their influence on the surrounding media is important from the point of view of earthquake-resistant design [1]. Alternative applications are in the fields of quantitative ultrasonics [2, 3]. More specifically, acoustic waves penetrate the material in question and are scattered by various types of defects, leading to a number of important and interesting problems that may be understood quantitatively only in terms of semi-analytical and numerical techniques. Among these application problems we mention the development of effective structural integrity monitoring and non-destructive testing evaluation techniques for quality control of materials and structural elements. Since the partial differential equation governing SH-wave motion is scalar, the displacement vector which has a single component perpendicular to the plane of wave propagation may be identified with a potential function. This opens the gate to go beyond elastic waves to acoustic and water waves, so that high performance numerical tools for solving of SH-wave boundary-value problems (BVP) can be used in the fields of acoustics and ocean engineering.

In general, SH-waves can be used in the quantification of ground motion phenomena that transcends earthquake engineering [4]. Thus, it is possible to also study the dynamic response of buildings and bridges, as well as of infrastructure to blast-induced overpressure and to high wind loads, which are problems of considerable interest to contemporary engineering practice. Often enough, the presence of the surrounding soil must be taken into account. For this category of problems, the BIEM is a valuable numerical tool since it can handle semi-infinite media with high accuracy and minimal modeling effort [5].

Scattering and diffraction of elastic SH-waves by cavities and dynamic stress concentration in the neighborhood of a given cavity has been the subject of numerous analytical, semi-analytical and numerical investigations, see [6, 7, 8, 9, 10, 11, 12, 13]. More specifically, this antiplane wave motion problem was treated analytically using the wave function expansion method of Mow and Pao [6], by Lee [7] and more recently by Liang *et al.* [13]. Other techniques include matched asymptotic expansions that are applicable in the low frequency range [8] and the method of complex functions [14]. Among the various computational methods used, the BIEM seems to be

Received 15 June 2012,
accepted 3 December 2013.

© S. Hirzel Verlag · EAA

the most effective since we have (a) a reduction of the problem dimensionality because only surfaces need to be modeled in contrast with 'domain' methods such as finite elements; (b) the possibility to model lateral inhomogeneity and anisotropy directly by defining the appropriate Green's functions; (c) the solution at selected internal domain points is expressed in terms of boundary values without recourse to domain discretization; (d) the semi-analytical character of the method insofar as it is based on exact (and not approximate) Green's functions guarantees high accuracy; and (e) good quality in the numerical results since quadrature techniques are directly applied to the boundary integral equations that are an exact mathematical statement for the problem under consideration. This last comment extends to the modeling of infinite or semi-infinite domains because Sommerfeld's radiation condition is automatically satisfied with no need to construct special viscous boundaries.

Regarding in-plane wave motions, scattering and diffraction of P- and SV-waves is again considered in [6]. Following the seminal papers by Cruse [15], Cruse and Rizzo [16], Cruse [17] on a Laplace-transformed, direct-type BIEM elastodynamic formulation, a series of results using BIEM formalism appeared for the diffraction of planar elastic waves by cavities (see [18, 9, 19, 20, 21, 22] among others). Furthermore, Ohutsu and Uesugi [10] and Luco and DeBarros [11] developed an indirect-type BIEM to analyze planar wave scattering in a half-plane with surface relief plus a buried cavity. The presence of the free surface can be either treated by discretization that is followed by imposition of the boundary conditions as in the previous papers, or through the derivation of a specialized Green's function [23, 24]. If the latter path is followed, then evaluation of surface integrals along the free surface is unnecessary.

One basic difficulty encountered with the BIEM is derivation of problem-specific Green's functions. If this can be done, then a smaller set of boundary data appears in conjunction with the surface representations, which in turn requires fewer boundary elements for the discretization process. Whether or not this increases accuracy and reduces overall CPU execution time and memory requirements is problem-dependent, given the fact that computation of problem-specific Green's functions is in general more complex as compared to the conventional Green's function for the elastic full-space. In general, Green's functions for a given differential operator are known for relatively few simple cases of geometry and boundary conditions [25]. This is the main reason why most BIEM work on wave scattering uses the displacement formulation based on fundamental solutions for point forces in the full space obtained by Fourier transform. Disadvantages of this formulation include: (a) introduction of 'infinite' boundary elements at the edge of the free surface mesh, (b) disctretization of the surfaces marking heterogeneities in the interior; (c) degeneration of the BIEM solution if cracks are present in the continuum [15]; (d) if the background medium is anisotropic or continuously inhomogeneous, fundamental solutions for the corresponding partial differential equation cannot be obtained by the use of the Fourier transform.

This state of affairs acts was the motivation for the present authors to develop a non-hypersingular, traction-based BIEM based on a Green's function obtained by the Radon transformation for an orthotropic elastic half-plane for solving problems involving time-harmonic SH-waves. This formulation has the potential to include buried cracks, besides cavities and inclusions of arbitrary shape.

The traction-based BIE can be derived in two basic ways:

i) Use of the Betti-Rayleigh reciprocal elastodynamic theorem, which leads to a hypersingular formulation, since spatial derivatives appear in the traction fundamental solution. This renders the traction kernels in the surface integrals non-integrable. The only way to overcome this difficulty is to apply a regularization technique. Most regularization techniques known in the literature use partial integration to shift the derivatives from the traction fundamental solution tensor to the displacement vector. Consequently, the now regularized traction BIE has the same type of singularities as those appearing in the conventional displacement BIE, see [26].
ii) It is possible to employ a rather simple, straightforward approach based on the two-state conservation integrals of elasto dynamics, which leads directly to a non-hypersingular, traction based BIE, where the singular integrals are of Cauchy principle-value (CPV) type. This approach has been elaborated in [27], where the BIEM implementation for wave scattering by cracks is based on the use of constant (i.e., single node) boundary elements.

To the authors' best knowledge, a BIEM formulation for solution of wave motion problems in a half-plane with cavities of arbitrary shape and based on (i) a traction boundary integral formulation and (ii) using a Green's function for anisotropic half-plane behavior derived analytically by the Radon transform does not exist at present in the literature. This development allows for solution of a wider class of problems involving wave propagation and scattering in composite materials, in multifunctional materials, in cases where a material gradient is present and for general types of anisotropy. Thus, the results obtained herein can be used as benchmark examples for calibrating alternative numerical solutions of complex BVP. Briefly, the paper is structured as follows. First, the definition of the boundary-value problem (BVP) and the BIEM formulations in terms of both displacements and tractions are given in section 2. Section 3 presents all the numerical simulations, starting with detailed validation results and followed by a comprehensive set of results obtained for a series of representative examples. Finally, section 4 lists a set of conclusions.

In sum, the motivation behind this work is to develop, validate and apply advanced BIEM computational tools for wave propagation and scattering problems in the anisotropic half-plane with different type of discontinuities, including the possibility of stationary cracks. As

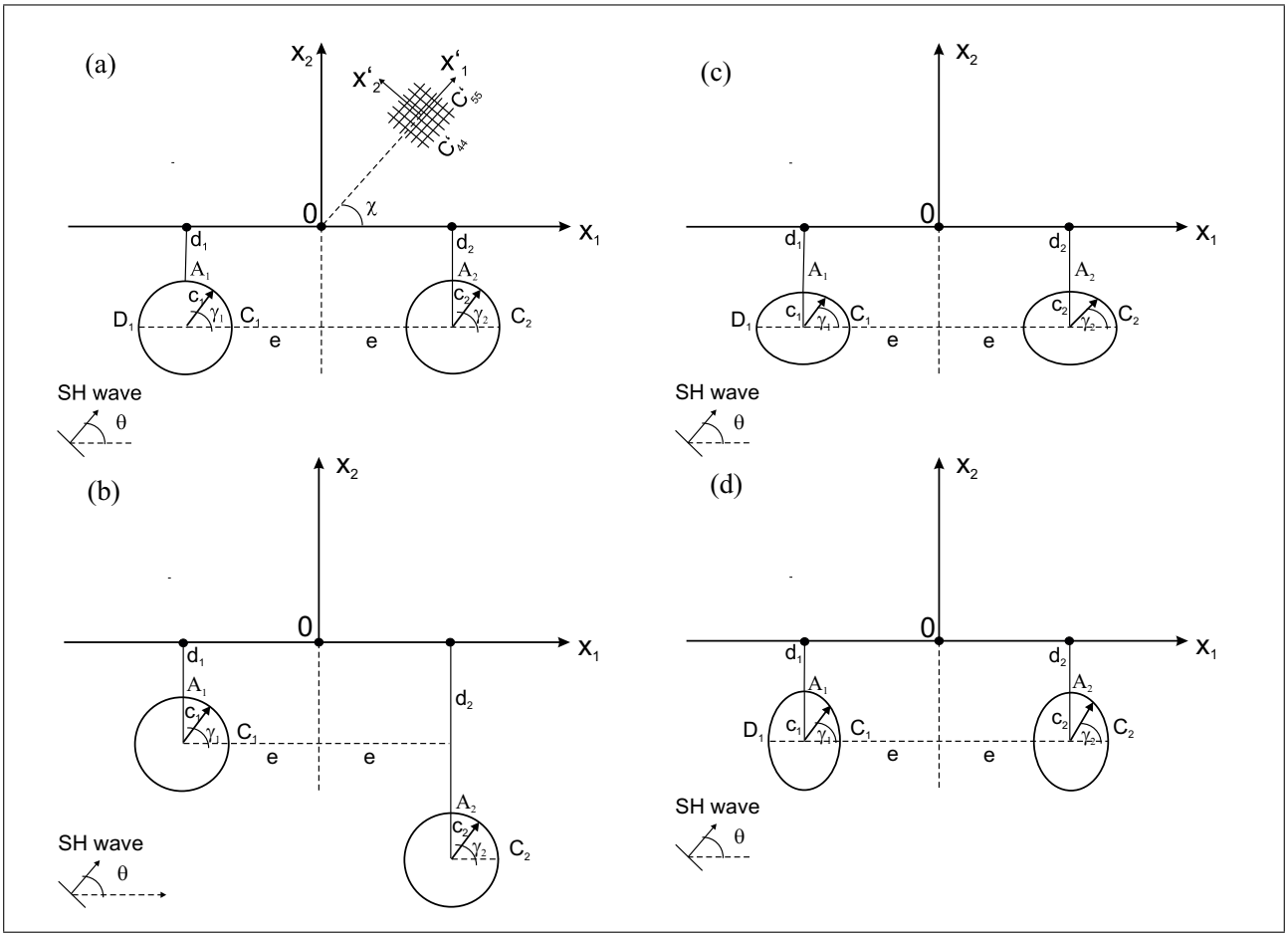


Figure 1. The problem geometry with four basic configurations for the cavities.

such, the proposed numerical approach is a continuation of the authors' previous efforts in this field, see [28, 29, 30].

2. Statement of the problem

Consider an orthotropic half-space containing a number of cylindrical cavities with constant cross sections and with axes at prescribed depths below the ground surface. The cavities are assumed to be infinitely long so that the wave field is identical in every plane section normal to their axes and thus the 3D problem reduces to a 2D one. The BIEM we propose has the potential to consider cavities of any number and shape, but in what follows we restrict ourselves to the case of two circular cavities H_i, $i = 1, 2$, $H_i \subset R^2_- = \{(x_1, x_2) : x_2 < 0\}$, with radius and depth c_i, d_i respectively and $H_1 \cap H_2 = \not{0}$. We will, however, include the case of elliptic cavities in the simulations to demonstrate the generality of our BIEM. In a Cartesian coordinate system $Ox_1x_2x_3$, the 2D model to be studied is shown in Figure 1 for different cavity scenarios. The medium is swept by time-harmonic SH-waves, polarized along the Ox_3 axis and propagating in the plane $x_3 = 0$, i.e., anti-plane motion is considered. In this case, the only non-zero quantities are displacement component $u_3(x, \omega)$ and shear stress components $\sigma_{i3}(x, \omega)$, $i = 1, 2$, at point $x = (x_1, x_2)$. The wave has frequency content ω and traces an incident angle θ with respect to the Ox_1 axis. Due to the time-harmonic behaviour of all variables, the common multiplier $e^{i\omega t}$ is suppressed in the following. The material properties of the elastic anisotropic homogeneous half-space are characterized by the positive elastic constants c_{44}, c_{55} and mass density ρ. We study the case when angle χ between the coordinate axis Ox_1 and the principle axis of material symmetry Ox'_1 is zero, i.e., the axes of the Cartesian coordinate system coincide with the principle directions of material symmetry, resulting the case of orthotropic anisotropy. If the solid is transversely isotropic and the axis of material symmetry is along the Ox_3 axis, then $c_{44} = c_{55} = \mu$ are satisfied and the plane x_3 is isotropic. Following Zhang and Gross [27], we introduce the notations $C_{11} = c_{44}$, $C_{22} = c_{55}$, $C_{12} = C_{21} = 0$ in order to simplify the formulas given below.

In the absence of body forces the orthotropic media is described in the frequency domain by the equation of motion, where the summation convention over repeated indices is implied and comma subscripts denote partial differentiation.

$$\sigma_{i3,i} + \rho\omega^2 u_3 = 0. \tag{1}$$

The constitutive law and the strain-displacement relations are

$$\sigma_{i3} = C_{ij} e_{j3}, \quad e_{i3} = u_{3,i}, \tag{2}$$

where e_{i3} is the strain.

The traction-free boundary condition is satisfied along the free surface $x_2 = 0$ and along the k-th cavity's boundary ∂H_k, i.e.,

$$t_3(x,\omega)\big|_{x_2=0} = 0, \quad t_3(x,\omega)\big|_{\partial H_k} = 0, \quad k = 1,2, \tag{3}$$

where the traction is $t_3(x,\omega) = \sigma_{i3}(x,\omega)n_i(x)$ and $n(x) = (n_1(x), n_2(x))$ is the outward pointing normal vector.

The BVP defined by equations (1), (3) for an incident SH-wave is solved using both the direct displacement and the non-hypersingular traction BIEM formulations that are based on the analytically derived Green's function for an orthotropic half-plane.

2.1. Incident wave in the half-plane in

The interaction of an incident wave u_3^{in} with the cavities produces scattered waves u_3^{sc}. The total wave field for displacements and tractions can be written as a sum of incident and the scattered wave fields

$$u_3 = u_3^{\text{in}} + u_3^{\text{sc}} \quad \text{and} \quad t_3 = t_3^{\text{in}} + t_3^{\text{sc}}. \tag{4}$$

The scattered wave is unknown and must satisfy the equation of motion equation (1), the boundary conditions equation (3) and a Sommerfeld-type condition at infinity on R_-^2.

The incident wave is the free-field ground motion, i.e., the wave field in the orthotropic half-plane without any cavities comprising incident and reflected by the free-surface SH-waves with incident angle θ and amplitude $|u_{30}|$. The displacement and traction free-field at a given point $x = (x_1, x_2)$ are evaluated by application of the superposition principle, see [31], and are as

$$u_3^{\text{in}}(x,\omega) = u_{03}\left[\mathrm{e}^{-\mathrm{i}k(\cos\theta x_1 + \sin\theta x_2)} + \mathrm{e}^{-\mathrm{i}k(\cos\theta x_1 - \sin\theta x_2)}\right], \tag{5}$$

$$\begin{aligned} t_3^{\text{in}}(x,\omega) = \mathrm{i}u_{03}k\Big[&\big(n_1 C_{11}\cos\theta + n_2 C_{22}\sin\theta\big) \\ &\cdot \mathrm{e}^{-\mathrm{i}k(\cos\theta x_1 + \sin\theta x_2)} \\ &+ \big(n_1 C_{11}\cos\theta - n_2 C_{22}\sin\theta\big) \\ &\cdot \mathrm{e}^{-\mathrm{i}k(\cos\theta x_1 - \sin\theta x_2)}\Big]. \end{aligned} \tag{6}$$

In the above, k is the wave number for the orthotropic case depends on θ, as $k = \omega/C_{\text{SH}}$,

$$C_{\text{SH}} = \sqrt{(C_{11}\cos^2\theta + C_{22}\sin^2\theta)/\rho},$$

see [32]. For the isotropic case, k is independent of θ, $C_{\text{SH}} = \sqrt{\mu/\rho}$, $k = \omega\sqrt{\rho/\mu}$ and in equations (5), (6) we replace C_{11} and C_{22} with μ.

2.2. Green's function

Our next aim is to derive Green's function for the orthotropic half-plane R_-^2 with traction-free conditions on $x_2 = 0$. We start with a fundamental solution $u_3^*(x,\xi)$, $(x,\xi) \in R_-^2 \times R_-^2$ defined as solution of equation (1) under a unit point load P^*, i.e.,

$$\sigma_{i3,i}^* + \rho\omega^2 u_3^* = -P^*\delta(x-\xi), \tag{7}$$

where $\sigma_{i3,i}^* = C_{ij}u_{3,j}^*$. We use the Radon transform, see [33] and follow the methods of Wang and Achenbach [34] for the anisotropic in-plane case and of Manolis *et al.* [30] for the anisotropic anti-plane case. The displacement fundamental solution in closed form is

$$u_3^*(x,\xi) = \frac{1}{4\pi^2}\int_{|m|=1} K(\hat{u}_3^*)(\beta,m)\big|_{\beta=|\langle x-\xi,m\rangle|}\,\mathrm{d}m, \tag{8}$$

where

$$\begin{aligned} K(\hat{u}_3^*)(\beta,m) = -\frac{1}{2C(m)}\Big\{&\mathrm{i}\pi\mathrm{e}^{\mathrm{i}k(m)\beta} \\ &- 2\Big[ci\big(k(m)\beta\big)\cos\big(k(m)\beta\big) \\ &+ si\big(k(m)\beta\big)\sin\big(k(m)\beta\big)\Big]\Big\}, \end{aligned} \tag{9}$$

and $C(m) = C_{ij}m_{ij}$, $k(m) = \omega\sqrt{\rho/C(m)}$. The derivatives of the fundamental solution with x are

$$\begin{aligned} u_3^{*x}(x,\xi) = \frac{1}{4\pi^2}\int_{|m|=1} &K_{,\beta}(\hat{u}_3^*)(\beta,m)\big|_{\beta=|\langle x-\xi,m\rangle|} \\ &\cdot m_j \operatorname{sgn}\big\langle x-\xi, m\big\rangle\,\mathrm{d}m. \end{aligned} \tag{10}$$

Now, define the Green's function $G_3^*(x,\xi)$, $(x,\xi) \in R_-^2 \times R_-^2$ using superposition as

$$G_3^*(x,\xi) = u_3^*(x,\xi) + u_3^*(x,'\xi), \quad x' = (x_1, -x_2). \tag{11}$$

Function $G_3^*(x,\xi)$ is a solution of equation (7), and for the corresponding traction $T^{*x} = C_{ji}G_{3,i}^{*x}n_j$ on $x_2 = 0$ we get

$$T^{*x}\big|_{x_2=0} = C_2\big[u_{3,2}^{*x}(x,\xi) - u_{3,2}^{*x}(x,\xi)\big]\big|_{x_2=0} = 0. \tag{12}$$

The Green's function G_3^* obtained here can also be recovered in alternative form using the fundamental solutions with full space anisotropy given in [27] and in [35]. These fundamental solutions are obtained by the Fourier transform and are expressed in terms of Bessel functions. It should be mentioned here that for the displacement-based BIEM, use of the Fourier transform Green's function is preferable. The reverse, however, is true for the the traction-based BIEM, the reason being that the Radon transform Green's function has a singular part which remains unchanged for any value of its argument and equal to that of the static case. This results in a computational advantage, since the Fourier transformed Green's function, composed by Hankel functions only asymptotically yields the same simple form for small arguments.

In closing, the Radon transform is a more general approach for obtaining fundamental solutions, and this is true if one moves into 2D in-plane anisotropy involving P and SV wave motion.

2.3. Boundary integral equations

Based on the closed-form Green's function of section 2.2, both displacement and non-hypersingular traction boundary integral equation formulations that are equivalent to the BVP defined by equations (1)–(3) are obtained below.

Although the solutions u3 obtained by both BIEM formulations are theoretically equivalent, for numerical simulation purposes we can evaluate stress concentration factors (SCF) m ore accurately using the later BIEM, while for evaluation of free surface and cavity displacements it is better to use the former BIEM.

Let Ω_R be a semi-circular domain with large radius R that includes two cavities and Ω_ε^1, Ω_ε^2 are small nonintersecting neighborhoods of these two cavities. Let us assume that when $R \to \infty$ and $\varepsilon \to 0$, then $\partial\Omega_\varepsilon^1 \to \partial H_1$, $\partial\Omega_\varepsilon^2 \to \partial H_2$.

(i) Using the dynamic equivalent to Somigliana's identity [18] and Somerfeld 's radiation condition (giving that the integrals over $\partial\Omega_R$ go to zero for $R \to \infty$), the following displacement BIEM is obtained for the scattered wave, see [36]

$$\alpha u_3^{\mathrm{sc}}(x) = -\int_\Gamma G_3^*(x,\xi) t_3^{\mathrm{in}}(\xi)\,\mathrm{d}\Gamma_\xi - \int_\Gamma T_3^*(x,\xi) u_3^{\mathrm{sc}}(\xi)\,\mathrm{d}\Gamma_\xi, \tag{13}$$

where $\alpha = 0.5$, $\Gamma = \partial H_1 \cup H_2$ and x, ξ are the observation and source points, respectively. Due to the boundary condition of equation (3), we use $t_3^{\mathrm{sc}}(\xi) = -t_3^{\mathrm{in}}(\xi)$ on Γ and $t_3^{\mathrm{in}}(\xi)$ is given in equation (6). Once the unknown $u_3^{\mathrm{sc}}(\xi)$ on Γ is found, the total wave field is given by equation (4) for every internal point $x \in R_-^2$ after usage of the integral representation formulae. Note that the scattered field on the free surface $x_2 = 0$ is obtained from equation (13) with $\alpha = 1$, because across $x_2 = 0$ we have $G_3^* = 2u_3^*$.

(ii) Using the the integral representation formulae for the displacement gradient $u_{3,i}^{\mathrm{sc}}$, see [27], and the conservation J-integral of linear elastodynamics with the boundary conditions of equation (3), the following non-hypersingular traction BIE is obtained,

$$0.5 t_3^{\mathrm{in}}(x) = C_{ji}(x) n_j(x) \int_\Gamma \Big[\Big(\Sigma_{3\eta}^*(x,\xi) u_{3,\eta}^{\mathrm{sc}}(\xi) - \rho\omega^2 G_3^*(x,\xi) u_3^{\mathrm{sc}}(\xi)\Big)\delta_{\lambda i} - \Sigma_{3\lambda}^*(x,\xi) u_{3,i}^{\mathrm{sc}}(\xi)\Big] n_\lambda(\xi)\,\mathrm{d}\Gamma_\xi + C_{ji}(x) n_j(x) \int_\Gamma G_{3,i}^*(x,\xi) t_3^{\mathrm{in}}(\xi)\,\mathrm{d}\Gamma_\xi, \tag{14}$$

where $\Sigma_{3j}^* = C_{ji} G_{3,i}^*$, $\Gamma = \partial H_1 \cup H_2$ and x, ξ are the position vectors of the observation and source points, respectively. Once the unknown displacement $u_3^{\mathrm{sc}}(\xi)$ on Γ is found, the scattered stress wave field at every internal point $x \in R_-^2$ is calculated from

$$u_3^{\mathrm{sc}}(x) = -\int_{\partial H} T_3^*(x,\xi) u_3^{\mathrm{sc}}(\xi)\,\mathrm{d}\partial H - \int_{\partial H} G_3^*(x,\xi) t_3^{\mathrm{in}}(\xi)\,\mathrm{d}\partial H, \tag{15}$$

$$\sigma_{3i}^{\mathrm{sc}}(x) = \int_\Gamma \Big[\Big(\Sigma_{3\eta}^*(x,\xi) u_{3,\eta}^{\mathrm{sc}}(\xi) - \rho\omega^2 G_3^*(x,\xi) u_3^{\mathrm{sc}}(\xi)\Big)\delta_{\lambda i} - \Sigma_{3\lambda}^*(x,\xi) u_{3,i}^{\mathrm{sc}}(\xi)\Big] n_\lambda(\xi)\,\mathrm{d}\Gamma_\xi + \int_\Gamma G_{3,i}^*(x,\xi) t_3^{\mathrm{in}}(\xi)\,\mathrm{d}\Gamma_\xi. \tag{16}$$

For points on the ground surface $x_2 = 0$ we use equation (15), because for such points both components of G_3^* satisfy equation (7), that giving a coefficient of 1 for $u_3^{\mathrm{sc}}(x)$ in equation (15) for $x = (x_1, 0)$.

3. Numerical solutions

3.1. Numerical procedure

The BIEM numerical procedure utilizes both the displacement equation (13) and the non-hypersingular traction, equation (14) formulations. Discretization of all surfaces rise yields numerical implementation through nodal collocation, and the resulting algorithms where validated by the authors (see [30], for a BIEM based on the fundamental solution for the full plane). Following nodal collocation with numerical evaluation of all integrals in equations (13), (14), an algebraic system of equations with respect to displacements along the cavity surfaces is obtained. The singular integrals converge in the CPV sense. They are solved analytically using the asymptotic behavior of the displacement and traction kernels for small arguments. The regular integrals are evaluated numerically using Gauss quadrature for onedimensional integrals and a quasi Monte Carlo method for solution of double integrals.

Two numerical codes were developed, one using Mathematica and the other Fortran for both the displacement and traction BIEM formulations. Typical sizes for the meshes following discretization of all surfaces include: (a) constant boundary elements: 30, 62, 130, 190 and 250 units; (b) quadratic boundary elements: 62, 130 and 190 units. The solutions are closer to the reference solution when the mesh is finer than 130 constant or 62 quadratic boundary elements. The percentage difference observed between solutions obtained by the displacement and the traction BIEM never exceeded 7–8% for comparable mesh sizes. From now onwards, all numerical results presented in the figures below are obtained by the traction BIEM.

As discussed in section 1, the non-hypersingular traction BIEM, in contrast to displacement BIEM, has the potential to model discontinuities in the form of cracks. The present Green's function avoids discretization of the free surface with corresponding decrease in the number of unknowns and consequently a smaller size for the matrix system of algebraic equations. To the best of our knowledge, there are no published results for cavities by either the displacement or the non-hypersingular traction BIEM for an orthotropic half-plane.

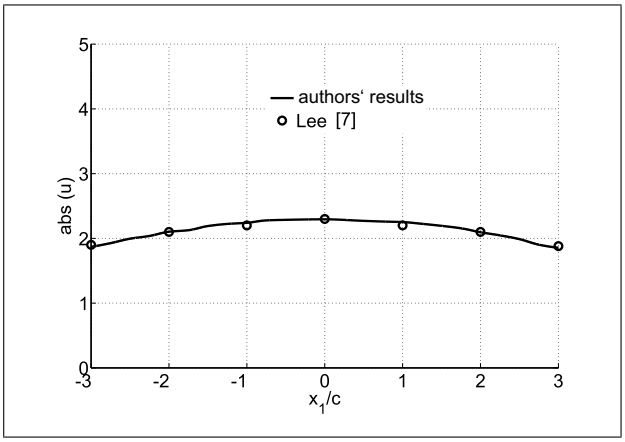


Figure 2. Surface displacement amplitude for a homogeneous elastic isotropic half-plane with a single cavity of radius c at depth $d = 5c$ subjected to SH incident wave with non-dimensional frequency $\eta = 0.5$ and incident angle $\theta = \pi/2$.

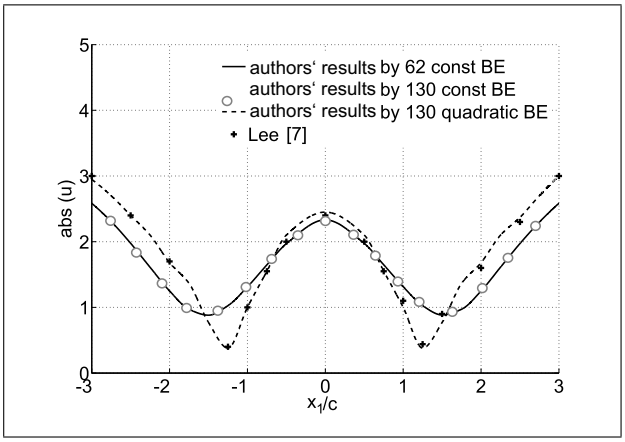


Figure 3. Surface displacement amplitude for half-plane with a single cavity of radius c at depth $d = 1.5c$ subjected to SH incident wave with non-dimensional frequency $\eta = 0.5$ and incident angle $\theta = \pi/2$.

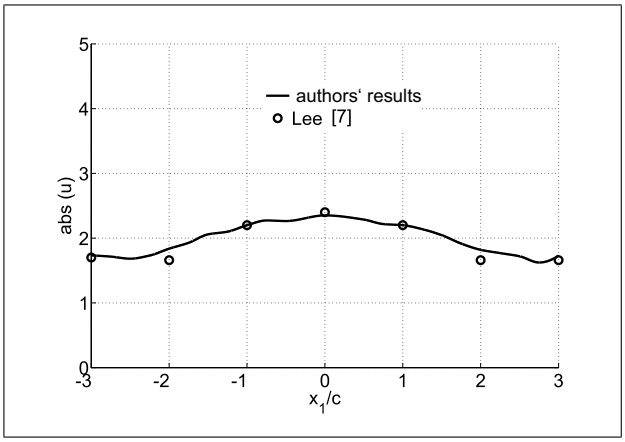


Figure 4. Surface displacement amplitude for a half-plane with a single cavity of radius c at depth $d = 5c$ subjected to SH incident wave with non-dimensional frequency $\eta = 1.0$ and incident angle $\theta = \pi/2$.

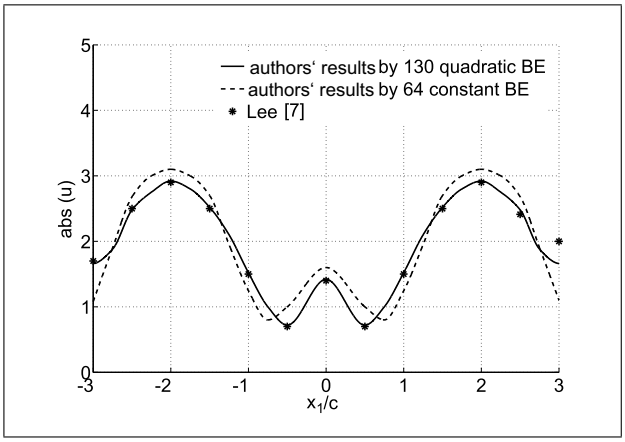


Figure 5. Surface displacement amplitude for a half-plane with a single cavity of radius c at depth $d = 1.5c$ subjected to SH incident wave with non-dimensional frequency $\eta = 1.0$ and incident angle $\theta = \pi/2$.

3.2. Validation study

The proposed methodology and its numerical implementation is validated by comparison with results available in the literature. Lee [7] was the first to present extensive numerical results for an infinite cylindrical cavity of radius c buried in an elastic isotropic half-plane at depth d and subjected to SH-waves at various angles of incidence θ. In order to validate our numerical methodology, we assume the axis of material symmetry is along the Ox_3-axis and then $c_{44} = c_{55} = \mu$, so that the plane $x_3 = 0$ is isotropic. We next introduce a non-dimensional frequency defined as the ratio of the cavity's diameter $2c$ to the wavelength λ_{SH}, namely $\eta = \omega c/(\pi C_{\mathrm{SH}}) = 2c/\lambda_{\mathrm{SH}}$.

Figures 2–5 compare the non-hypersingular traction BIEM results (see item (ii), section 2.3) for a single cavity with Lee [7] solutions for surface displacement amplitude versus x_1/c in the case of normal wave incidence, i.e. $\theta = \pi/2$. In these figures we use the notation $\mathrm{abs}(u_3) = \mathrm{abs}(u)$ for the displacement amplitude $|u_3^{\mathrm{in}} + u_3^{\mathrm{sc}}|$. More specifically, Figures 2 and 4 illustrate the results when cavity depth is $d = 5c$ and the non-dimensional frequency is $\eta = 0.5$ and $\eta = 1.0$, respectively. Also, the distribution of the displacement amplitude for the case when the cavity depth is $d = 1.5c$ is presented in Figures 3 and 5 at two different frequencies $\eta = 0.5$ and $\eta = 1.0$. We should note that the usage of quadratic boundary elements lead to results closer to those in [7].

Next, Figures 6–8 compare the obtained results with those of Lee [7] for the same problem as before, but for an incidence angle $\theta = \pi$ and for the following cases: (a) $\eta = 0.5$, $d = 5c$, or $d = 1.5c$ in Figures 6 and 7 respectively; (b) $\eta = 1.0$ and $d = 5c$ in Figure 8. The comparisons of results obtained by quite different computational techniques show that all solutions converge, see Figures 2, 4, 6 -8 and that any detectable differences occur for some isolate points in Figures 3 and 5.

Finally, Figure 9 demonstrates the effect of embedment depth d on the dynamic response at the traction-free surface under normal wave incidence ($\theta = \pi/2$) and for three

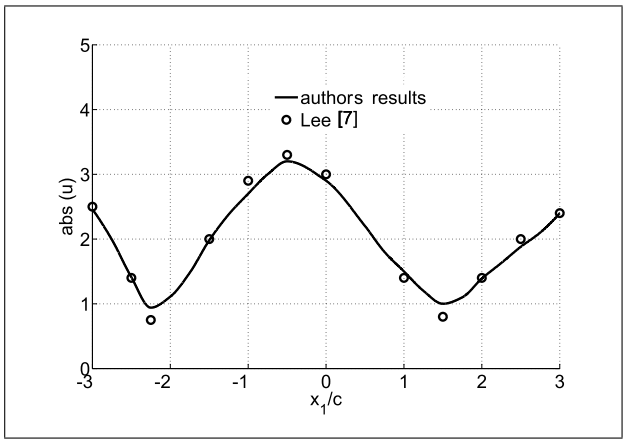


Figure 6. Surface displacement amplitude for a half-plane with a single cavity of radius c at depth $d = 5c$ subjected to SH incident wave with non-dimensional frequency $\eta = 0.5$and incident angle $\theta = \pi$.

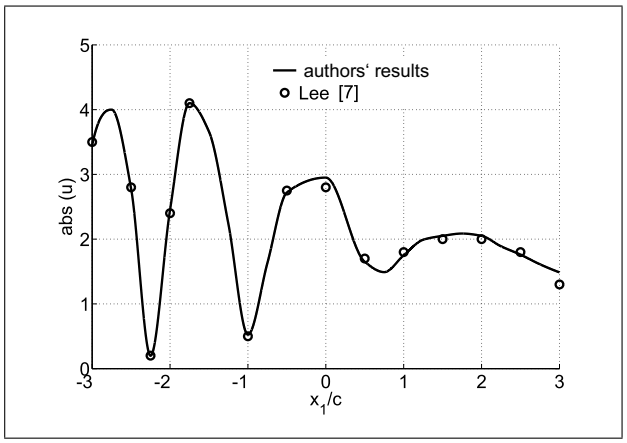


Figure 7. Surface displacement amplitude for a half-plane with a single cavity of radius c at depth $d = 1.5c$ subjected to SH incident wave with non-dimensional frequency $\eta = 0.5$ and incident angle $\theta = \pi$.

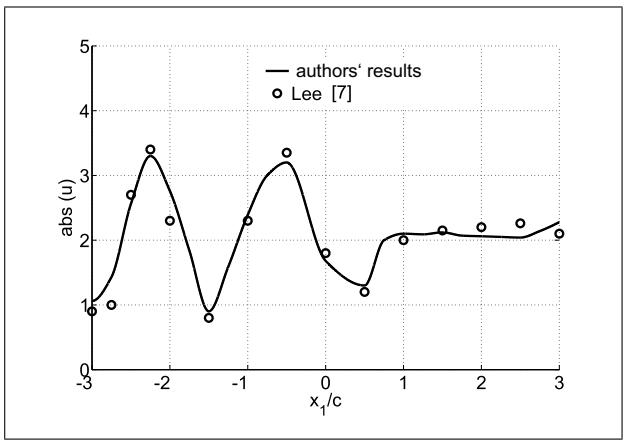


Figure 8. Surface displacement amplitude for a half-plane with a single cavity of radius c at depth $d = 5c$ subjected to SH incident wave with non-dimensional frequency $\eta = 1.0$ and incident angle $\theta = \pi$.

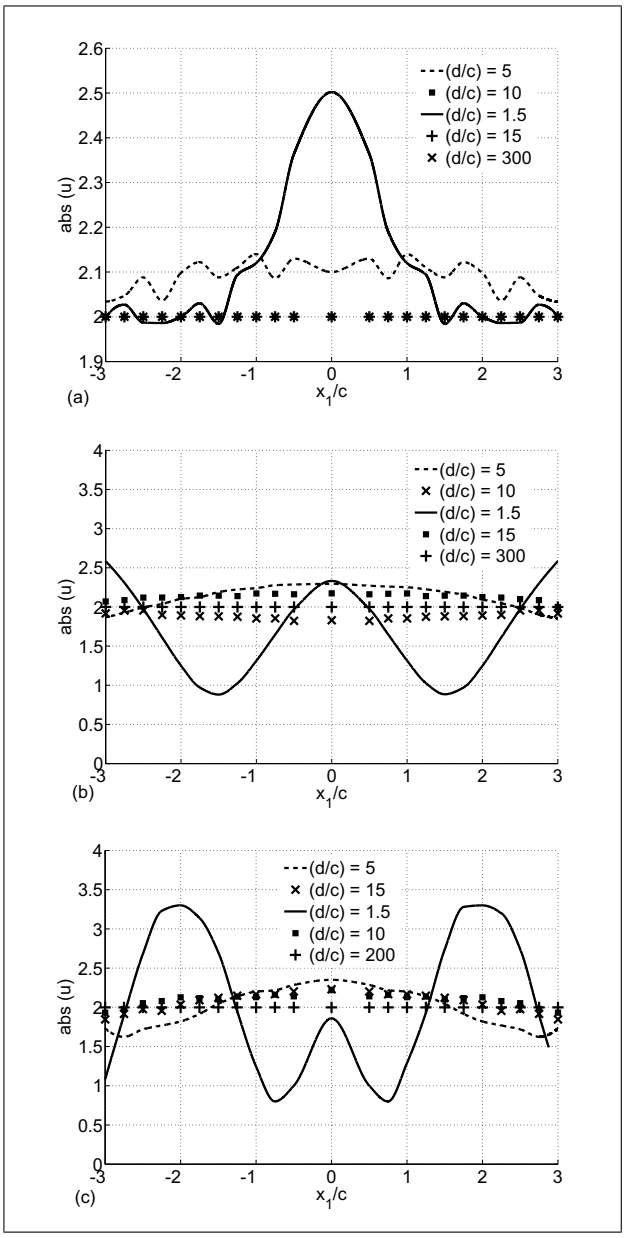


Figure 9. Surface displacement amplitude versus x_1/c for different ratios d/c and incident angle $\theta = \pi/2$ at three different normalized frequencies: (a) $\eta = 0.1$; (b) $\eta = 0.5$; (c) $\eta = 1.0$.

different normalized frequencies of $\eta = 0.1$, $\eta = 0.5$ and $\eta = 1.0$. Also, five depth to radius ratios d/c are compared. As this ratio increases, the total displacement along the free surface approaches that of the free-field response without a cavity, which is nothing more than the amplitude of the incident wave. It can be seen that when $d = 200c$, the displacement amplitude of the total wave field at all observer points is approximately equal to 2.0. Also, when the ratio d/c increases, the presence of a free surface on the cavity below is negligible. In the se cases, the dynamic response of a cavity practically is identical to that of a cavity in an infinite plane. In contrast, as the ratio d/c decreases, the effect of the free surface becomes noticeable. This effect is frequency dependent, as can be seen in Figure 9. Higher non-dimensional ratios lead to greater complexity

of the wave field, but this complexity is mitigated by increasing the depth to radius ratio of the cavity.

A key variable when cavities interact is the SCF, defined as the ratio of the stress at a point along the circumference to the maximum amplitude 0 of the incident wave's stress component at that same point, see [6]. The normalized dynamic SCF $|\sigma_{\theta\gamma}/\tau_0|$ is computed as

$$\begin{aligned} \sigma_{\theta\gamma} &= -\sigma_1 \sin(\theta-\gamma) + \sigma_2 \cos(\theta-\gamma), \\ \sigma_i &= \sigma_{i3} + \sigma_{i3}^{\text{in}}, \end{aligned} \tag{17}$$

where $\tau_0 = \mathrm{i}\omega u_0 \sqrt{c_{44}\rho}$ is the amplitude of the maximum shear stress of the incident SH-wave with unit amplitude u_0 for the elastic isotropic case. Also, γ is the angle that the observation point traces along the cavity boundary and θ is the incident wave angle, see Figure 1. As a validation test, we compute SCF at point A_1 ($\gamma = \pi/2$) of a single cavity in the isotropic half-plane versus normalized frequency $\Omega = \omega c C_{\text{SH}}^{-1} = \eta\pi$ for incident wave angle $\theta = 0$ and depth of burial $d = 100c$, see Figure 10. As already discussed before, the influence of the free surface can be neglected for this case and we expect that the SCF distribution approaches that for a cavity in an infinite plane. Thus, we can compare with the result of Mow and Pao [6]. Good quality results are obtained by both the present non-hypersingular traction BIEM for a deep cavity and by the displacement BIEM for a cavity in the infinite plane by using the fundamental solution for the full space.

Finally, the displacement amplitude at the left rim ($\gamma = \pi$) of a single cavity versus normalized frequency η in the case of normal SH-wave incidence ($\theta = \pi/2$) and depth of burial $d = 2c$ is shown in Figure 11, where we compare with results by Liang *et al.* [13]. The results obtained by two very different computational techniques, as is the traction BIEM and the wave function expansion method of Liang *et al.* [13] is further proof that our numerical scheme is accurate. Continuing along these lines, the results for surface displacement amplitude versus x_1/c for two cavities with radius c, depth $d = 2c$ and separation distance $e = 10c$ is given in Figure 12. The incident SH-wave characteristics are $\theta = \pi/2$ and $\eta = 0.5$. With increasing separate distance e, the interaction between cavities becomes negligible and the solution converges to the case of a single cavity. This tendency can be seen in Figure 12, where the results obtained in the case $e = 10c$ match the authors' solution for a single cavity and those obtained by Lee [7].

3.3. Parametric study

In what follows, we conduct a parametric study to investigate the sensitivity of the wave field in a elastic isotropic/othotropic half-plane with two cavities of radius c and subjected to incident SH-wave. The study is presented with respect to the following parameters: the angle θ and frequency ω of incident plane SH-wave; the ratio of cavity's diameter to length of the incident wave; the ratio d/c of depth of cavity from ground surface to radius; and ratio e/c of the separation distance between cavities to their radius. At first, Figures 13 and 14 reveal the influence

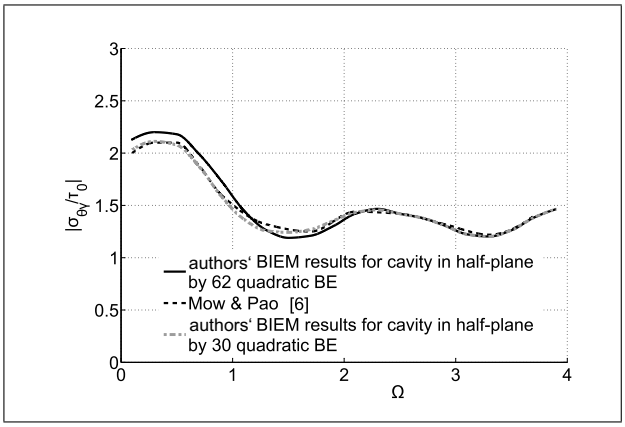


Figure 10. SCF at point A_1 ($\gamma = \pi/2$) along a single cavity with $d = 100c$ versus normalized frequency of SH-wave with incident angle $\theta = 0$. Comparison with Mow and Pao [6] for a circular hole in a homogeneous elastic isotropic infinite plane.

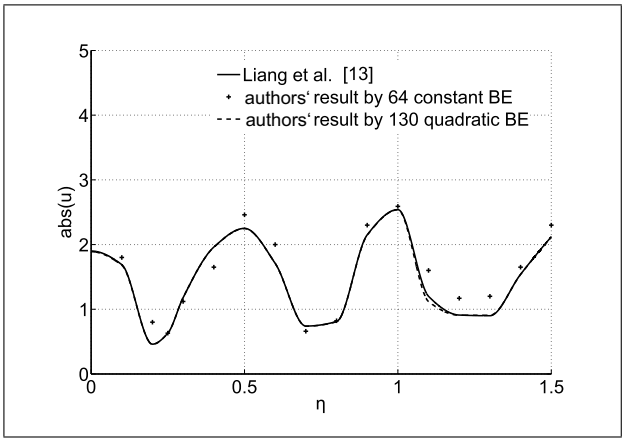


Figure 11. Displacement amplitudes at left rim ($\gamma = \pi$) point along a single cavity of radius c and depth $d = 2c$ versus dimensionless frequency η of incident normal SH-wave propagating in a half-plane. Comparison with Liang *et al.* [13].

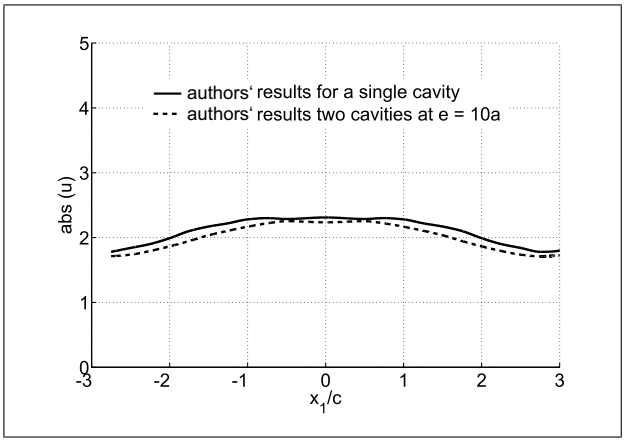


Figure 12. Surface displacement amplitude versus x_1/c in the case of two cavities (Figure 1a) with radius c, depth $d = 2c$ and separate distance $e = 10c$ due to incident SH-wave with non-dimensional frequency $\eta = 0.5$ and incident wave angle $\theta = \pi/2$.

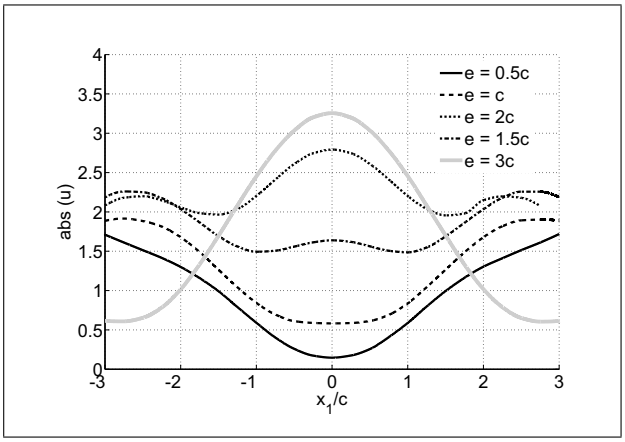


Figure 13. Surface displacement amplitude versus x_1/c in the case of two cavities (Figure 1a) with radius c, depth $d = 2c$ and different separation distances e due to incident SH-wave with non-dimensional frequency $\eta = 0.4$ and incident wave angle $\theta = \pi/2$.

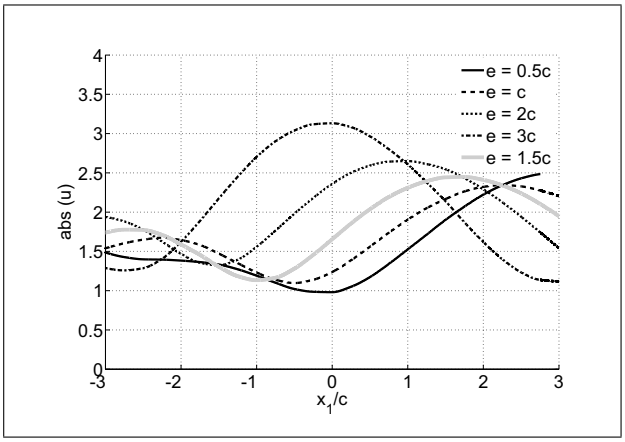


Figure 14. Surface displacement amplitude versus x_1/c in the case of two cavities (Figure 1b) with radius c, depths $d = 2c$, $d = 5c$ and different separation distances e due to incident SH-wave with non-dimensional frequency $\eta = 0.4$ and incident wave angle $\theta = \pi/2$.

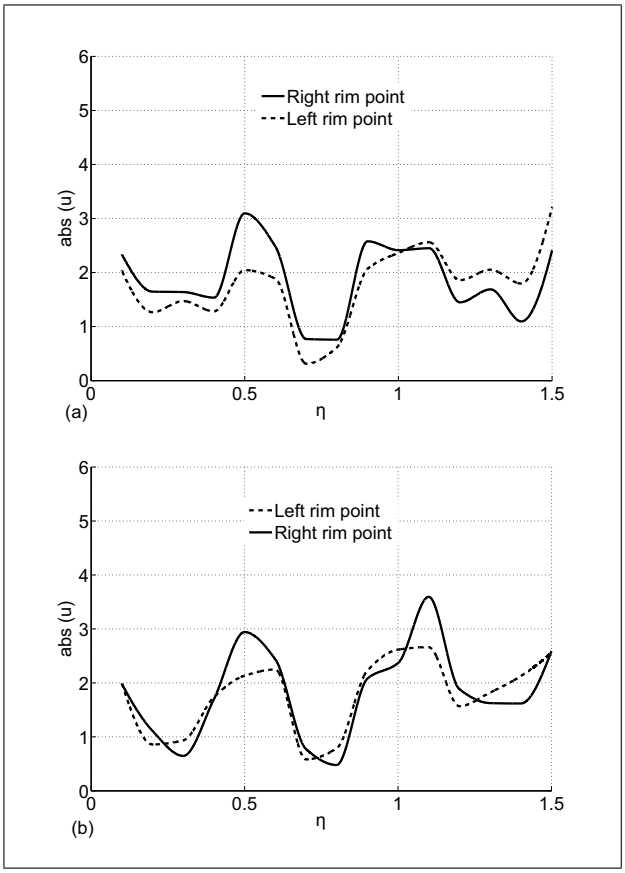


Figure 15. The case of two cavities situated at depth $d = 2c$, see Figure 1a. Displacement amplitude at the right and left rim points C_1 ($\gamma = 0$) and D_1 ($\gamma = \pi$) along the first cavity with center $O(-e - c_1, -d_1)$ versus normalized frequency η of normal SH-wave: (a) $e = 0.5c$; (b) $e = 2c$.

of both: ratio e/c and configuration of the cavities in the half-plane with respect to the incident wave orientation. Figure 13 represents the configuration given in Figure 1a, where the ratio $d/c = 2$, while Figure 14 is for the geometry given in Figure 1b , where $d_1 = 2c$ and $d_2 = 5c$. In both figures the incident angle is $\theta = \pi/2$ and the dimensionless frequency is $\eta = 0.4$. By decreasing the separation distance e between the cavities, the wave pattern changes rapidly and differs considerably with what is observed for the original reference configurations. For instance, we observe instances of doubling or even tripling of the free surface amplitude when the cavities are in close proximity.

In Figure 15 we consider the same basic scenario as before, but the results are shown now for displacement amplitudes at the right ($\gamma = 0$) and left ($\gamma = \pi$) rim points along the left cavity with center $O_1(-e - c, -d_1)$. These figures clearly demonstrate the influence of cavity configuration, of ratio e/c for the normalized separation distance between cavities, and the dynamic interaction between cavities and free surface. All these factors generate a rather complex wave field in the half-plane. For instance, the higher values for displacements at the right rim (the point closest to the second cavity), which is sometimes more than triple the reference case value, illustrate the dynamic interaction between cavities.

The shape of the cavity is another important factor that can change the resulting wave field. Figure 16 plots the distribution of the surface displacement amplitude along the free surface for non-dimensional frequency $\eta = 0.4$ and incident wave angle $\theta = \pi/2$, when two elliptic cavities at depth $d = 2c$ are situated in the half-plane. The separate distance between these cavities is $e = 0.5c$ or $e = 2c$. In Figure 16a, the ellipses are configured so that semi- axis c is horizontal and semi-axis $c/2$ is vertical, while in Figure 16b the orientation of the two semi-axis is reversed. The rapid change in the wave field picture due to this reversal of orientation, plus the fact that the cavities are now elliptic, is clearly visible. Again, we observe amplification and deamplification factors in the surface displacements that may range from 3.5 to 0.2, respectively. Obviously this type of information cannot be deduced by practical considerations alone.

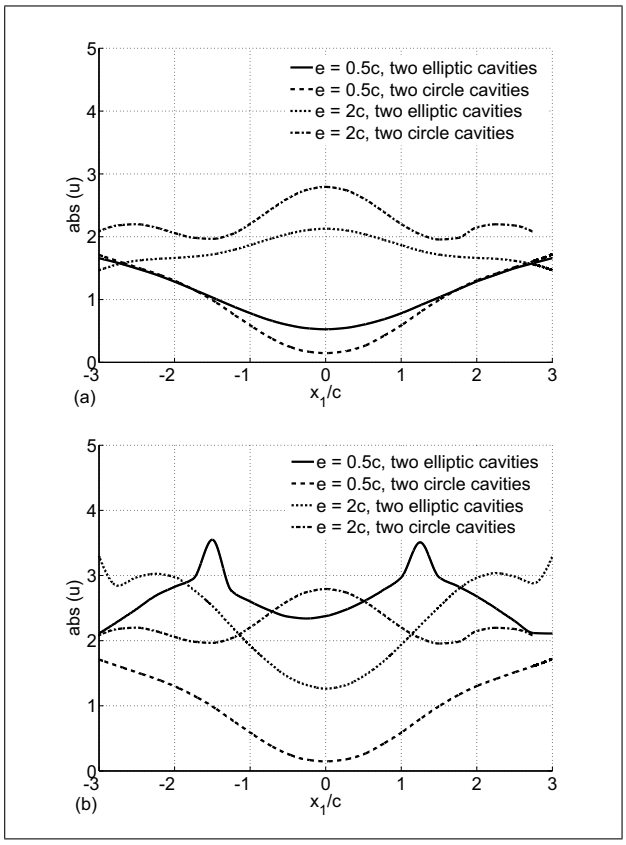


Figure 16. Surface displacement amplitude versus x_1/c for two elliptic cavities with $d = 2c$ and separation distance e due to incident SH-wave with non-dimensional frequency $\eta = 0.4$ and incident wave angle $\theta = \pi/2$: (a) semi-axis c (horizontal) and semi-axis $c/2$ (vertical), see Figure 1c; (b) semi-axis $c/2$ (horizontal) and semi-axis c (vertical), see Figure 1d.

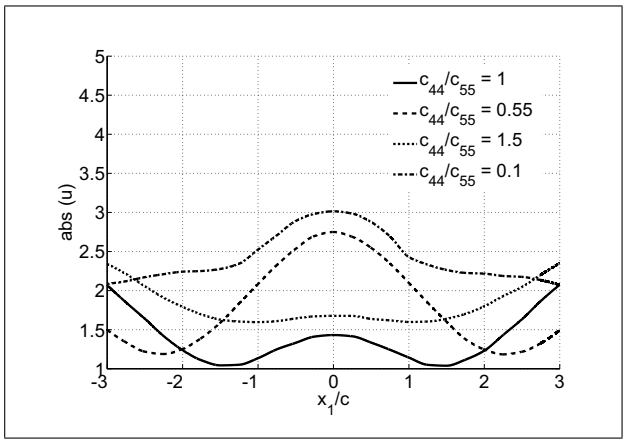


Figure 17. Surface displacement amplitude versus x_1/c for a single cavity in an orthotropic half-plane, see Figure 1a, with radius c and depth $d = 2c$ subjected to SH-wave with non-dimensional frequency $\eta = 0.4$ and incident angle $\theta = \pi/2$.

Figures 17 and 18 finally show the influence of material orthotropy on the dynamic response of the half-space with cavities. In both figures, the incidence angle is $\theta = \pi/2$ and the dimesionless frequency is fixed at a value $\eta = 0.4$. Figures 17 and 18 respectively correspond to a single circular cavity and two circular cavities (Figure 1a) with radius c and depth $d = 2c$. A comparison between elastic isotropic ($c_{44}/c_{55} = 1$) and the following elastic orthotropic cases is presented, where $c_{44}/c_{55} = 0.1$; 0.55; 1.5. The mutual interplay of material anisotropy, with cavity-to-cavity interaction can strongly influence the computed wave field. It is obvious that the presence of anisotropy also creates high amplification / de-amplification situations that yield factors of up to 3 and 0.5, respectively. It should be noted finally that the ratio $c_{44}/c_{55} = 0.1$ is not realistic, as it shows a great mismatch of stiffness in two principle directions that does not occur in typical materials; it is merely shown for completeness purposes.

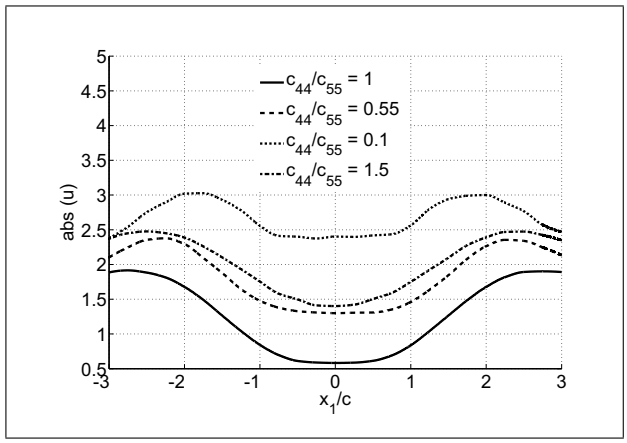


Figure 18. Surface displacement amplitude versus x_1/c for two cavities in an orthotropic half-plane, see Figure 1b, with radius c and depth $d = 2c$ subjected to SH-wave with non-dimensional frequency $\eta = 0.4$ and incident angle $\theta = \pi/2$.

4. Conclusions

The time-harmonic problem of an infinite, homogeneous orthotropic half-space weakened by cavities of arbitrary shape and excited by upwards propagating SH-waves was addressed here by the BIEM. More specifically, two formulations were considered, namely a displacement BIEM and a non- hypersingular traction BIEM that were both based on a Green's function for the orthotropic half-plane obtained by the Radon transformation. These formulations were implemented numerically and required discretization of the cavity surfaces only, thus leading to a substantial reduction in size of the system matrices obtained following standard nodal collocation procedure. Next, the well-known benchmark problem for SH-wave diffraction by a single cavity in the isotropic half-plane was solved and the results obtained were validated against those from the literature. Following this, extensive numerical simulations for two cavities revealed the development of a complex wave field in the vicinity of the free surface directly above, which depends on the interplay of cavity-surface geometry, degree of material anisotropy, plus frequency content and directivity of the incoming SH-wave signal. Future work will be in the direction of multiple lined cavities with

internal pressure, plus the introduction of a second liquid phase in the surrounding soil so as to represent poroelasticty. These refinements are important in earthquake engineering, whereby the dynamic response of the built urban environment is a first step in devising methods to mitigate the seismically-induced risk. Other applications can be found in the field of mechanics and include the acoustic properties of panels with holes, the dynamic response of composite materials containing multiple inclusions, etc.

Acknowledgement

The first author (PD) wishes to acknowledge support provided through the MC-IEF grant PIEF-GA-2010-270889. The re maining authors wish to acknowledge financial support provided through the NATO Collaborative Linkage Grant No. 984136 and the German Research Foundation grant DFG-Wu496/5-1.

References

[1] R. Villaverde: Fundamental concepts of earthquake engineering. CRC Press, Boca Raton, Florida, 2009.

[2] L. M. Brekhovskikh, O. A. Godin: Acoustics of layered media. I: Plane and quasi-plane problems. Springer, Berlin, 1990.

[3] L. M. Brekhovskikh, O. A. Godin: Acoustics of layered media. II: Point sources and bounded beams. Springer, Berlin, 1992.

[4] M. L. Baron, H. H. Bleich, P. Weidling: Theoretical studies on ground shock phenomena. The Mitre Corporoation, Bedford, Massachusetts, 1960.

[5] J. Dominguez: Boundary elements in dynamics. Computational Mechanics, Southampton, 1993.

[6] C. C. Mow, Y. H. Pao: Diffraction of elastic waves and dynamic stress concentration. Crane Russak, New York, 1971.

[7] V. W. Lee: On deformation near circular underground cavity subjected to incident plane SH-waves. – In: Proceedings Application of Computer Methods in Engineering Conference. C. Wellford (ed.). University of South California, Los Angeles, 1977, 951–962.

[8] S. K. Datta, A. H. Shah: Scattering of SH-waves by embedded cavities. Wave Motion **4** (1982) 256–283.

[9] S. Kobayashi: Some problems of the boundary integral equation method in elastodynamics. – In: Boundary Elements V. C. A. Brebbia, T. Futagami, M. Tanaka (eds.). CMP, Southampton, 1983, 775–784.

[10] M. Ohutsu, S. Uesugi: Analysis of sh wave scattering in a half-space and its applications to seismic responses of geological structures. Eng. Anal. **2** (1985) 198–204.

[11] J. E. Luco, F. C. DeBarros: Dynamic displacements and stresses in the vicinity of a cylindrical cavity embedded in a half-space. Earthq. Eng. Struct. Dyn. **23** (1994) 321–340.

[12] J. Liang, Z. Liu: Diffraction of plane SV waves by a cavity in poroelastic half-space. Earthq. Eng. Eng. Vibr. **8** (2009) 29–46.

[13] J. Liang, L. Hao, V. Lee: Difraction of plane SH waves by a semi-circular cavity in half-plane. Earthq. Sci. **23** (2010) 5–12.

[14] D. Liu, B. Gai, G. Tao: Applications of the method of complex functions to dynamic stress concentrations. Wave Motion **4** (1982) 293–304.

[15] T. A. Cruse: A direct formulation and numerical solution of the general transient elastodynamic problem. II. J. Math. Anal. Appl. **22** (1968) 341–355.

[16] T. A. Cruse, F. J. Rizzo: A direct formulation and numerical solution of the general transient elastodynamic problem. I. J. Math. Anal. Appl. **22** (1968) 244–259.

[17] T. A. Cruse: Two-dimensional BIE fracture mechanics analysis. Appl. Math. Modell. **2** (1978) 287–293.

[18] G. D. Manolis, D. E. Beskos: Dynamic stress concentration studies by boundary integrals and Laplace transform. Int. J. Num. Meth. Eng. **17** (1981) 573–599.

[19] Y. Niwa, S. Hirose, M. Kitahara: Application of the boundary integral equation method to transient response analysis of inclusions in a half-space. Wave Motion **8** (1986) 77–91.

[20] C. P. Providakis, D. A. Sotiropoulos, D. E. Beskos: BEM analysis of reduced dynamic stress concentration by multiple holes. Commun. Numer. Meth. Eng. **9** (1993) 917–924.

[21] H. G. Georgiadis, A. P. Rigatos, N. C. Charalambakis: Dynamic stress concentration around a hole in a viscoelastic plate. Acta Mech. **111** (1995) 1–12.

[22] G. Rus, R. Gallego: Boundary integral equation for inclusion and cavity shape sensitivity in harmonic elastodynamics. Eng. Anal. Bound. Elem. **29** (2005) 77–91.

[23] M. Kinoshita: Master of Science Thesis (in Japanese; quoted in kobayashi, 1983). Department of Civil Engineering, Kyoto University, Kyoto, Japan, 1983.

[24] D. P. N. Kontoni, D. E. Beskos, G. D. Manolis: Uniform half-plane elastodynamic problems by an approximate boundary element method. Soil Dyn. Earth Eng. **6** (1987) 227–238.

[25] E. Kausel: Fundamental solutions in elastodynamics: A compendium. Cambrige University Press, Cambrige, 2006.

[26] V. Sladek, J. Sladek: Transient elastodynamic three-dimensional problems in cracked bodies. Appl. Math. Model. **8** (1984) 2–10.

[27] C. Zhang, D. Gross: On wave propagation in elastic solids with cracks. Computational Mechanics, Southampton, 1998.

[28] P. Dineva, F. Wuttke, G. Manolis: Elastic wave scattering and stress concentration effects in non-homogeneous poroelastic geological media with discontinuities. Soil Dyn. Earthq. Eng. **41** (2012).

[29] T. V. Rangelov, G. D. Manolis, P. S. Dineva: Elastodynamic fundamental solutions for certain families of 2D inhomogeneous anisotropic domains: Basic derivations. Europ. J. Mech. A/Solids **24** (2005) 820–836.

[30] G. D. Manolis, P. S. Dineva, T. V. Rangelov: Dynamic fracture analysis of a smoothly inhomogeneous plane containing defects by BIEM. Eng. Anal. Bound. Elem. **36** (2012) 727–737.

[31] R. Courant, D. Hilbert: Methods of Mathematical Physics. Vol. II. Wiley, New York, 1962.

[32] C. Zhang, D. Gross: Interaction of anti-plane cracks with elastic waves in transversely isotropic materials. Acta Mech. **101** (1993) 231–247.

[33] A. Zayed: Handbook of generalized function transformations. CRC Press, Boca Raton, Florida, 1996.

[34] C. Y. Wang, J. D. Achenbach: Elastodynamic fundamental solutions for anisotropic solids. Geophys. Int. J. **118** (1994) 384–392.

[35] C. H. Daros: On modelling SH-waves in a class of inhomogeneous anisotropic media via the boundary element method. ZAMM – Z. Angew. Math. Mech. **90** (2010) 113–121.

[36] A. Saez, J. Dominguez: BEM analysis of wave scattering in transversely isotropic solids. Int. J. Numer. Meth. Eng. **44** (1999) 1283–1300.